

# Bar-formation as driver of gas inflows in isolated disc galaxies

R. Fanali<sup>1</sup>, M. Dotti<sup>1,2</sup>, D. Fiacconi<sup>3</sup> & F. Haardt<sup>4,2</sup>

<sup>1</sup> *Università degli Studi di Milano Bicocca, I-20126 Milano, Italy*

<sup>2</sup> *INFN, Sezione di Milano–Bicocca, Piazza della Scienza 3, I-20126 Milano, Italy*

<sup>3</sup> *Institute for Computational Science, University of Zürich, Winterthurerstrasse 190, CH-8057 Zürich, Switzerland*

<sup>4</sup> *DiSAT, Università dell’Insubria, via Valleggio 11, I-22100 Como, Italy*

September 30, 2015

## ABSTRACT

Stellar bars are a common feature in massive disc galaxies. On a theoretical ground, the response of gas to a bar is generally thought to cause nuclear starbursts and, possibly, AGN activity once the perturbed gas reaches the central super-massive black hole. By means of high resolution numerical simulations we detail the purely dynamical effects that a forming bar exerts on the gas of an isolated disc galaxy. The galaxy is initially unstable to the formation of non-axisymmetric structures, and within  $\sim 1$  Gyr it develops spiral arms that eventually evolve into a central stellar bar on kpc scale. A first major episode of gas inflow occurs during the formation of the spiral arms while at later times, when the stellar bar is establishing, a low density region is carved between the bar co-rotational and inner Lindblad resonance radii. The development of such “dead zone” inhibits further massive gas inflows. Indeed, the gas inflow reaches its maximum during the relatively fast bar formation phase and not, as often assumed, when the bar is fully formed. We conclude that the low efficiency of long-lived, evolved bars in driving gas toward galactic nuclei is the reason why observational studies have failed to establish an indisputable link between bars and AGNs. On the other hand, the high efficiency in driving strong gas inflows of the intrinsically transient process of bar formation suggests that the importance of bars as drivers of AGN activity in disc galaxies has been overlooked so far. We finally prove that our conclusions are robust against different numerical implementations of the hydrodynamics routinely used in galaxy evolution studies.

**Key words:** galaxies: bulges — galaxies: nuclei — methods: numerical

## 1 INTRODUCTION

The fraction of disc galaxies showing a well developed stellar bar in the local Universe is substantial, up to  $\gtrsim 30\%$  for massive ( $M_* \gtrsim 10^{9.5} M_\odot$ ) systems (Laurikainen, Salo & Buta 2004; Nair & Abraham 2010; Lee et al. 2012a; Gavazzi et al. 2015). The effectiveness of bars in modifying the dynamics of gas has been recognized since decades (e.g. Sanders & Huntley 1976; Roberts, Huntley & van Albada 1979; Athanassoula 1992). In particular, gas within the bar corotational radius ( $R_C$ , i.e. the radius at which the angular velocity in the disc plane  $\Omega(R)$  equals the bar pattern precession speed  $\Omega_b$ ) is driven toward the centre of the galaxy because of the interaction with the bar itself. Early theoretical studies suggested that such inflows could be responsible for nuclear starbursts and, if the gas is able to reach the very central regions of the galaxy, AGN activity (e.g. Shlosman, Frank & Begelman 1989; Berentzen et al. 1998).

From the observational point of view the connection between bars and enhanced nuclear star formation has been extensively proved (e.g. Ho, Filippenko & Sargent 1997; Martinet & Friedli 1997; Hunt & Malkan 1999; Laurikainen, Salo & Buta 2004; Jogee, Scoville & Kenney 2005). The link between bars and AGN seems less clear: while barred galaxies host AGNs more frequently than their non-barred analogous (making bars a good candidate for the triggering of nuclear activity, e.g. Laurikainen, Salo & Buta 2004; Oh, Oh & Yi 2012), it is still matter of debate whether the presence of bars is one of the main drivers of AGNs (as suggested by, e.g. Knapen, Shlosman & Peletier 2000; Laine et al. 2002; Alonso, Coldwell & Lambas 2013) or not (see e.g. Ho, Filippenko & Sargent 1997; Mulchaey & Regan 1997; Hunt & Malkan 1999; Lee et al. 2012b; Cisternas et al. 2013; Cheung et al. 2015).

In order to have a comprehensive understanding of the gas dynamics in barred galaxies many numerical studies have been put forward, including, for example both 2- or 3-D simulations, and different schemes for the gas hydrodynamics (smoothed particle hydrodynamics, SPH, vs grid codes). We consider particularly meaningful to divide the different efforts in three main classes:

(i) **Isolated galaxies with analytical bars** (e.g. Athanassoula 1992; Regan & Teuben 2004; Kim, Seo & Kim 2012). In this class of simulations (often restricted to a 2-D geometry) bars are represented by analytical potentials that do not evolve in time (but for their rigid body rotation). These simulations, although quite idealized, allows for extremely high resolutions and precise evolution of the gas dynamics.

(ii) **Fully evolving isolated galaxies** (e.g. Berentzen et al. 1998, 2007; Villa-Vargas, Shlosman & Heller 2010; Cole et al. 2014), where bars are modeled (as the rest of the galaxy) as evolving structures, that can change their extents, rotational patterns, etc.

(iii) **Cosmological simulations** (e.g. Romano-Díaz et al. 2008; Scannapieco & Athanassoula 2012; Kraljic, Bournaud & Martig 2012; Goz et al. 2014; Fiacconi, Feldmann & Mayer 2015). In these simulations the galaxies form from cosmological perturbations, and are free to acquire mass and angular momentum through large scale gas inflows and galaxy mergers. In this approach the initial conditions are not arbitrary, but, because of the large boxes simulated (even in zoom-in runs), the spatial and mass resolution is usually significantly coarser than in isolated simulations.

Simulations of the first kind have confirmed the analytical prediction that, in many galactic potentials, bar-driven gas inflows fail to reach the very centre of the galaxy. The gas shocks around the outermost inner Lindblad resonance (ILR) radius ( $R_{\text{ILR}}$ ) of the bar, defined by the equality  $\Omega(R) - \kappa(R)/2 = \Omega_b$  where  $\kappa$  is the epicyclic frequency, i.e. the frequency of small radial oscillations. At  $R_{\text{ILR}}$  the gas shocks, forming nuclear rings that are often observed as star forming regions in barred galaxies (e.g. Kormendy 2013, and references therein). Simulations that fully evolve the bar potential do show similar results as soon as they reach a quasi-steady state, i.e. after the bar growth transient<sup>1</sup>. If the gas inflows accumulates enough mass at  $\sim R_{\text{ILR}}$  the central region can dynamically decouple, possibly forming nested non-axisymmetric structures (e.g. nuclear bars). These structures can eventually bring the gas closer and closer to the galactic centre in a cascade-like fashion (Shlosman, Frank & Begelman 1989).

In this paper we propose a new set of fully evolving isolated galaxies runs. We start with an unbarred galactic disc composed of stars and gas, embedded in an evolving dark matter halo. We check the dependences of the gas dynamics on different numerical implementations, varying the magnitude of an artificial viscosity (if present) and the numerical

resolution (see section 2.2 for a full description of the different runs). We run our simulations without implementing any gas radiative cooling, star formation and stellar feedback prescriptions (usually referred to as sub-grid physics), in order to perform a clean test of the basic numerical method used, and to highlight the physical and purely dynamical effect of the forming substructures (stellar spirals and bar) onto the gas.

As will be detailed we find that the flux of gas reaching the most central regions of the galaxy peaks during the bar formation phase, and not when the bar is fully established, independently of the exact numerical implementation. We describe in details the set-up of our initial conditions and the features of the simulation suite in Section 2. We present our main findings in Section 3, and we finally discuss them and derive our conclusions in Section 4, highlighting the relevance of our work for the interpretation of observations and also commenting on the possible shortcomings.

## 2 NUMERICAL METHODS

### 2.1 Initial conditions

We simulate the isolated disc galaxy model Lmd2c12 described by Mayer & Wadsley (2004), in order to reproduce an initially bulgeless, bar-unstable disc galaxy. The galaxy model is made of three different components: a dark matter halo, a stellar and a gaseous disc.

The dark matter halo follows the Navarro, Frenk & White (NFW 1996, 1997) density profile:

$$\rho_h(r) = \frac{\rho_{\text{crit}} \delta_c}{(r/r_s)(1 + r/r_s)^2}, \quad (1)$$

where  $r_s$  is the scale radius of the halo,  $\rho_{\text{crit}}$  is the critical density of the Universe today<sup>2</sup>, and:

$$\delta_c = \frac{200}{3} \frac{c^3}{\log(1+c) - c/(1+c)}, \quad (2)$$

depends only on the concentration parameter  $c \equiv r_{200}/r_s$ .  $r_{200}$  is the radius that encompasses an average density  $\langle \rho \rangle = 200 \rho_c$  and defines the outer radius of the dark matter halo. The mass of the halo is therefore  $M_{200} = 200 \rho_c (4\pi/3) r_{\text{vir}}^3$ . We adopt  $c = 12$  and a scale velocity  $v_{200} = \sqrt{GM_{200}/r_{200}} = 75 \text{ km s}^{-1}$ , which corresponds<sup>3</sup> to  $M_{200} = 1.4 \times 10^{11} M_\odot$ ,  $r_{200} = 110 \text{ kpc}$  and  $r_s = 9.2 \text{ kpc}$ .

Both stellar and gaseous discs are modeled as a radial exponential disc with a vertical structure modelled by isothermal sheets (Hernquist 1993):

$$\rho_*(R, z) = \frac{M_*}{4\pi R_*^2 z_*} \exp(-R/R_*) \cosh^{-2}\left(\frac{z}{z_*}\right), \quad (3)$$

where  $R_* = 3 \text{ kpc}$  is the radial scale length and  $z_* = 0.3 \text{ kpc}$  is the vertical scale height. The stellar disc has a total stellar

<sup>1</sup> Although promising, the coarse resolution of cosmological runs makes hard to fully resolve the nuclear region where the ILR is expected to occur.

<sup>2</sup> We assume  $H_0 = 71 \text{ km s}^{-1} \text{ Mpc}^{-1}$ , compatible with the *Wilkinson Microwave Anisotropy Probe* 7/9 years cosmology (Komatsu et al. 2011; Hinshaw et al. 2013)

<sup>3</sup> These numbers are slightly different from those reported by Mayer & Wadsley (2004) because of the different cosmology assumed. However, this does not affect the evolution of the galaxy model.

mass  $M_\star = 1.4 \times 10^{10} M_\odot$  and extends up to  $10R_\star$ . The gas component has a mass  $M_{\text{gas}} = 0.05M_\star = 7 \times 10^8 M_\odot$  and its density profile is characterized by the same parameters  $R_\star$  and  $z_\star$ . The gas has a uniform temperature  $T_0 = 10000$  K and we assume that it is composed of a mixture of ionized hydrogen and helium with a mean molecular weight  $\mu \simeq 0.59$ . All the parameters are chosen in agreement with the galaxy-halo scalings predicted by the  $\Lambda$ -CDM model (e.g. Mo, Mao & White 1998).

We build the initial conditions using the code GINCO<sup>4</sup>. GINCO initializes quasi-equilibrium galaxy models following Hernquist (1993) and Springel, Di Matteo & Hernquist (2005). The models can be made of four arbitrary components: a NFW dark matter halo, an exponential stellar and gaseous disc, and a spherical bulge with the profile proposed by Hernquist (1990). The polar/spherical coordinates of the particles that belong to each component are randomly sampled using the density profiles as probability distribution functions. Then, polar/spherical angles are randomly drawn from isotropic distributions and they are used to determine the Cartesian coordinates of the particle positions.

The velocities are sampled from local Gaussian approximations of the true distribution function (Hernquist 1993). The position-dependent parameters of the Gaussians are computed solving the steady-state Jeans equations with some closure assumptions on the velocity dispersion tensor (see e.g. Binney & Tremaine 2008). For spherical components (i. e. the dark matter halo, since the simulated system is bulgeless), we assume that the velocity dispersion tensor is isotropic (i.e. of the form  $\sigma^2(r)\mathbb{I}$ , where  $\mathbb{I}$  is the identity matrix), with the 1D velocity dispersion given by:

$$\sigma^2(r) = \frac{1}{\rho(r)} \int_r^{+\infty} \rho(x) \frac{d\Phi_{\text{tot}}}{dr}(x) dx, \quad (4)$$

where  $\rho(r)$  is the density profile of the considered component and  $\Phi_{\text{tot}}$  is the total gravitational potential. The spherical components have no net rotation. The potential of the halo is an analytic function; instead, the potential of the disc is computed as a first-order vertical perturbation of the potential of a razor-thin exponential disc, namely  $\Phi_d(R, z) \simeq \Phi_0(R) + \Phi_1(R, z)$ . The razor-thin disc has the potential:

$$\Phi_0(R) = -\frac{GM_\star}{R_\star} y [I_0(y)K_1(y) - I_1(y)K_0(y)], \quad (5)$$

where  $y = R/(2R_\star)$  and  $I_i$  and  $K_i$  are modified Bessel functions; the first-order vertical perturbation is (e.g. Binney & Tremaine 2008):

$$\begin{aligned} \Phi_1(R, z) &\equiv 4\pi G \int_0^z dz' \int_0^{z'} dz'' \rho_\star(R, z'') \\ &= 4\pi G \rho(R, 0) z_\star^2 \log \left[ \cosh \left( \frac{z}{z_\star} \right) \right]. \end{aligned} \quad (6)$$

We use this strategy to maintain all the evaluations of the potentials and of their derivatives analytic; this makes the code faster and reduces the required memory. Once we compute  $\sigma^2(r)$ , we can sample the magnitude of the velocity of

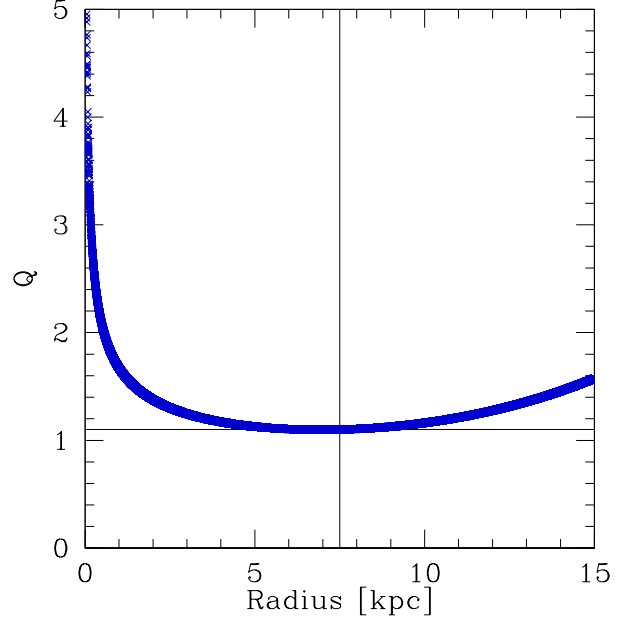


**Figure 1.** Radial profile for the Toomre parameter of the initial stellar disc.

each particle in a spherical component from a Maxwellian distribution with variance  $\sigma^2(r)$ . Finally, we randomly draw the spherical angles  $(\theta, \phi)$  as above to ensure isotropy and we assign the Cartesian components of the velocity.

Both the stellar and the gaseous disc velocity structure is characterized by a velocity dispersion tensor of the form  $\text{diag}(\sigma_r^2, \sigma_\phi^2, \sigma_z^2)$ . The vertical velocity dispersion is (Hernquist 1993; Springel, Di Matteo & Hernquist 2005):

$$\begin{aligned} \sigma_z^2(R, z) &= \frac{1}{\rho_\star(R, z)} \int_z^{+\infty} \rho_\star(R, z') \frac{\partial \Phi_{\text{tot}}}{\partial z}(R, z') dz' \\ &\approx \frac{GM_\star z_\star}{2R_\star^2} \exp \left( -\frac{R}{R_\star} \right), \end{aligned} \quad (7)$$

where the last approximation holds when the disc is geometrically thin and the vertical gradient of the potential around  $z \simeq 0$  is dominated by the disc. The radial component is chosen to be  $\sigma_r^2 \propto \sigma_z^2$ , with the normalization enforcing a minimum value of the Toomre parameter  $Q \simeq 1.1$  at  $r \simeq 2.5R_\star$  (Mayer & Wadsley 2004). The whole profile of  $Q$  for our initial conditions is shown in Fig. 1. The azimuthal component is set using the epicyclic approximation,  $\sigma_\phi^2 = \sigma_r^2 \kappa^2 / (4\Omega^2)$ . Unlike the dark matter halo, the disc has a net rotation, i.e. an average azimuthal velocity  $\langle v_\phi \rangle$  given by (Hernquist 1993; Springel, Di Matteo & Hernquist 2005):

$$\langle v_\phi \rangle^2 = V_c^2 + \sigma_r^2 \left( 1 - \frac{\kappa^2}{4\Omega^2} - \frac{2R}{R_\star} \right), \quad (8)$$

where  $V_c$  is the circular velocity in  $\Phi_{\text{tot}}$ . Finally, we sample the  $(v_r, v_\phi, v_z)$  components of the velocity of each disc (both star and gas) particles from gaussian distributions with mean  $(0, \langle v_\phi \rangle, 0)$  and standard deviations  $(\sigma_r, \sigma_\phi, \sigma_z)$ , respectively, and we finally transform then into the Cartesian components.

We checked the stability of our initial conditions studying the evolution of the stellar surface density profile as a function of time (left panel of Fig. 2) during the first Gyr, i.e.

<sup>4</sup> GINCO (Galaxy INitial COnditions, <http://www.ics.uzh.ch/~fiacconi/software.html>) was written by Davide Fiacconi.

before the development of strong non-axisymmetric perturbation (see below). After a short transient phase due to the non-exact equilibrium of the initial conditions (highlighted by the yellow line in figure) the system re-adjust on a profile similar to the initial one, with the surface density at  $t = 1$  Gyr (red line) differing by 20% at most with respect to the initial conditions (within the disc scalelength). Similar conclusions about the stability of the stellar disk can be drawn from the evolution of its Lagrangian radii (right panel of Fig. 2).

## 2.2 Simulation suite

We run a suite of numerical simulations of the reference model described in the previous Section in order to explore the effects of resolution, numerical implementation and parametrization of the artificial viscosity (when present). In Table 1 we summarize the sample of 3D runs presented in this work. We build two realizations of our initial conditions at two resolutions:

(i) low resolution (LR): the halo is sampled with  $10^6$  particles with mass  $m_h = 1.4 \times 10^5 M_\odot$ , while the stellar and gaseous discs are sampled with  $9.5 \times 10^5$  and  $5 \times 10^4$  particles, respectively, with mass  $m_\star = m_{\text{gas}} \simeq 1.5 \times 10^4 M_\odot$ . The gravitational softenings (setting the spatial/force resolution of the gravitational interaction) for dark matter and baryonic particles (equal for stars and gas particles) are 65 pc and 20 pc, respectively;

(ii) high resolution (HR): the halo is sampled with  $8 \times 10^6$  particles with mass  $m_h = 1.6 \times 10^4 M_\odot$ , while the stellar and gaseous discs are sampled with  $7.6 \times 10^6$  and  $4 \times 10^5$  particles, respectively, with mass  $m_\star = m_{\text{gas}} \simeq 1.7 \times 10^3 M_\odot$ . The gravitational softenings for dark matter and baryonic particles are 30 pc and 7 pc, respectively.

We ensure that the particles in the disc (star and gas) have all the same mass, preventing any spurious relaxation/mass segregation. All the simulations assume an isothermal equation of state to simply model an effective atomic radiative cooling keeping the ISM in the disc plane at an almost constant temperature  $\lesssim 10^4$  K. Metal line and molecular cooling would reduce the gas temperature further, allowing for dense clumps to form and to trigger star-formation. Feedback from stars would then re-heat the gas, resulting in the formation of a multi-phase medium (e.g. Wada 2001; Wada & Norman 2001). Because of the lack of cooling and star-formation physics, we keep an high temperature to prevent the sudden fragmentation of the gaseous disc.

We test the robustness of our results against two different implementations of the hydrodynamics. Most of the simulations are performed with the Tree/Smoothed Particle Hydrodynamics (SPH) code GADGET2 (Springel 2005), which uses an oct-tree structure to speed up the gravity calculations (Barnes & Hut 1986) and treats the hydrodynamics with the density-entropy SPH proposed by Springel & Hernquist (2002). The SPH formalism requires the introduction of an artificial viscosity in order to capture shocks correctly (e.g. Monaghan 1992; Balsara 1995; Monaghan 1997). Therefore, we explore the effect of different choices of the value of the artificial viscosity parameter

**Table 1.** Summary of simulations characteristics. Columns: (1) name of the simulation, (2-3) resolution, (4) code used, (5) artificial viscosity  $\alpha$ .

Name	Barion particle softening (pc)	DM particle softening (pc)	Code	$\alpha$
LR	20	65	GADGET2	0.8
LRV16	20	65	GADGET2	1.6
LRV04	20	65	GADGET2	0.4
LRGiz	20	65	GIZMO	-
HR	7	30	GADGET2	0.8

$\alpha^5$ . Finally, we also compare the results from SPH simulations with a run that uses the newly developed code GIZMO (Hopkins 2014). GIZMO is a meshfree code that captures advantages from both SPH and grid codes: it preserves the Lagrangian structure of SPH codes, but at the same time solved directly the Euler equations among different regions of the computational domain without requiring the implementation of any artificial viscosity. We used it in its finite-mass variant, in which there is not mass flux among the regions belonging to different particles, keeping the mass of each gas particle fixed.

## 3 RESULTS

### 3.1 Low resolution simulations

Figure 3 shows the distribution of star and gas observed in the LR run at three different times,  $t = 1, 4$  and 7 Gyr in the left, central and right panels respectively. The stellar surface density is shown in the upper and middle panels (edge-on and face-on views, respectively), while the face-on view of the gas surface density is shown in the lower panels. During the first 2 Gyr the bar-unstable system evolves from an axisymmetric configuration to a barred disc, passing through the formation of transient multi-arm spirals. In particular, a three arm spiral structure is observable in the stellar density distribution at  $t = 1$  Gyr in the left-middle panel of figure 3. From 2 Gyr on the disc shows a clear bar structure (with a size of about 8 kpc) in its central region. From the bar-formation time ( $t \approx 2$  Gyr) on, the bar tends to slow-down, as shown in the upper panel of figure 4. At  $t \lesssim 3$  Gyr the bar makes almost 2.8 full precessions per Gyr, while the frequency decreases down to  $\lesssim 2.3$  precessions per Gyr at  $t \approx 7$  Gyr. The bar slow-down, already extensively discussed in literature (e.g. Sellwood 1981; Combes & Sanders 1981; Halle et al. 2015), results in a  $R_{\text{ILR}}$  growing in time, from  $\sim 1$  kpc up to  $\sim 1.4$  kpc at the end of the run, as observable in the lower panel of figure 4. The bar forms thin, and buckles in its centre as the time goes by, as observable in the edge on view of the stellar disc at  $t = 4$  and 7 Gyr. At the end of the simulation a boxy-peanut bulge like structure is observable within the central few kpc of the disc.

The dynamics of the subdominant gas component is dominated by the underlying stellar dynamics. During the first 2 Gyr the gas distribution resembles the stellar one,

<sup>5</sup> The  $\beta$  parameter in the Monaghan-Balsara formulation is equal to  $2\alpha$  in all our runs.

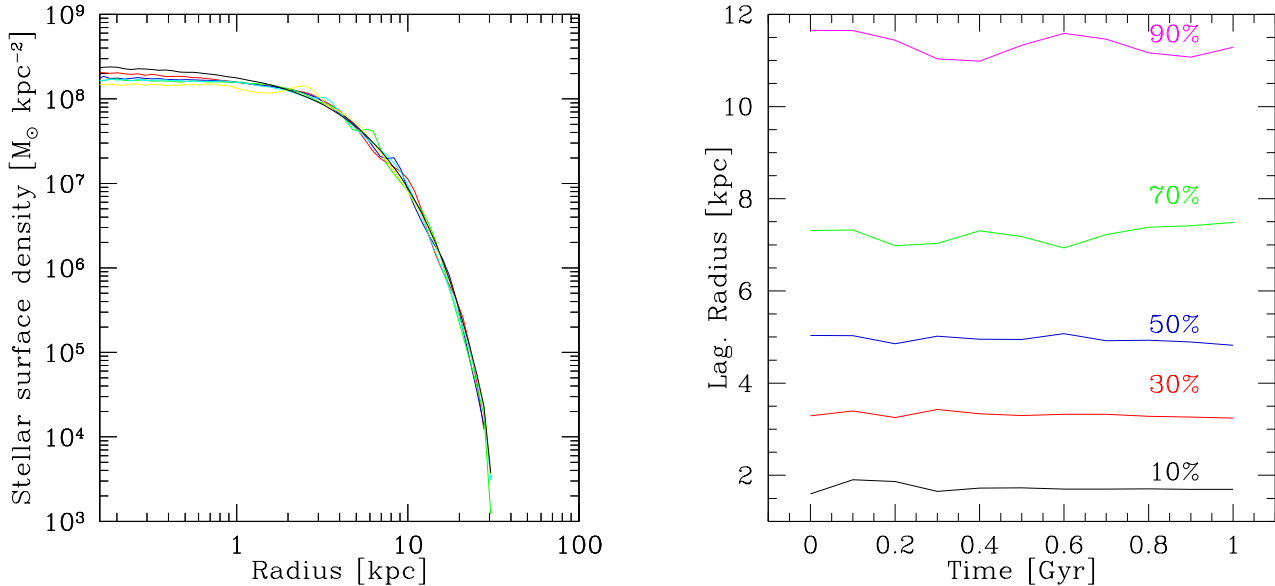


**Figure 2.** Left panel: surface density profile of the stellar component in the first Gyr. Black, yellow, cyan, green, blue and red curves correspond to  $t = 0, 0.2, 0.4, 0.6, 0.8$  and  $1$  Gyr, respectively. Right panel: lagrangian radius at different stellar mass fraction in the first Gyr. Black, red, blue, green and magenta lines represent 10%, 30%, 50%, 70%, 90% of stellar mass, respectively.

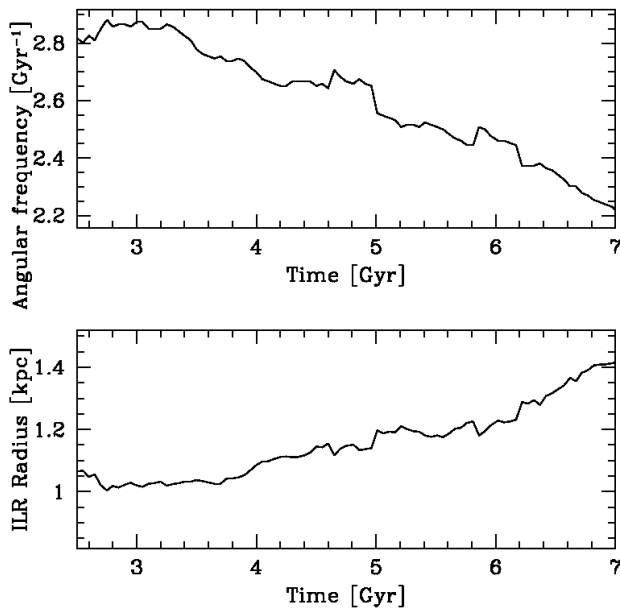


**Figure 4.** Angular frequency of the bar (upper panel) and radius corresponding to the inner Lindblad resonance from  $t = 2.5$  to  $t = 7$  Gyr (lower panel).

with clear spiral arms (almost co-spatial with the stellar ones) observable (see the example in the left lower panel of figure 3 at  $t = 1$  Gyr). After the formation of the stellar bar, the gas within the bar corotational radius ( $R_C \approx 4-5$  kpc depending on the age of the bar, as will be discussed below) is driven toward the galaxy centre, and forms a dense knot of gas clearly observable in the central and right panels in the bottom row of figure 3. The torquing effect of the spiral arms before and the stellar bar afterwards sweeps the almost

totality of the gas between  $R_C$  and the central dense knot. A small amount of low dense gas is still observable in this “dead region”, in particular in the form of two inflowing streams connecting the outer galactic disc with the central dense knot, often observed in simulations as well as in real galaxies (e.g. Regan, Sheth & Vogel 1999).

The left panel of figure 5 quantifies the effect that the bar formation process has onto the gas. The surface density of the gas in the dead zone decreases by up to  $\sim 1.5$  orders of magnitude at  $t \gtrsim 3$  Gyr (blue, yellow and red lines) with respect to the initial conditions (black line). The shaded areas in figure trace the evolution of  $R_C$  (green) and its outermost inner Lindblad resonance radius ( $R_{ILR}$  pink), from when a clear bar structure is observable and its angular frequency is measurable ( $t \approx 2$  Gyr) to the end of the simulation. The gas within  $R_C$  is dragged toward scales of the order of  $R_{ILR}$ , fueling the formation of the central knot of gas on sub-kpc scales (in agreement with a wealth of previous studies, e.g. Sanders & Huntley 1976; Shlosman, Frank & Begelman 1989; Athanassoula 1992; Berentzen et al. 1998; Regan & Teuben 2004; Kim, Seo & Kim 2012; Cole et al. 2014), where the surface density increases by up to almost 2 orders of magnitude.

A clear although less obvious result of the LR run consists in the efficiency of the “dead zone” formation. Most of the inflow from  $R < R_C$  to  $R \lesssim R_{ILR}$  happens during the first 2 Gyr, as observable comparing the cyan ( $t = 1$  Gyr), green ( $t = 2$  Gyr) and blue ( $t = 3$  Gyr) lines with the initial conditions and the end result of the simulation in the left panel of figure 5. The fully formed bar does indeed play a role in further decreasing the gas surface density on the dead zone, and most importantly, in preventing new gas to refill the central regions by pushing the gas immediately outside the CR toward the outer Lindblad resonance radius

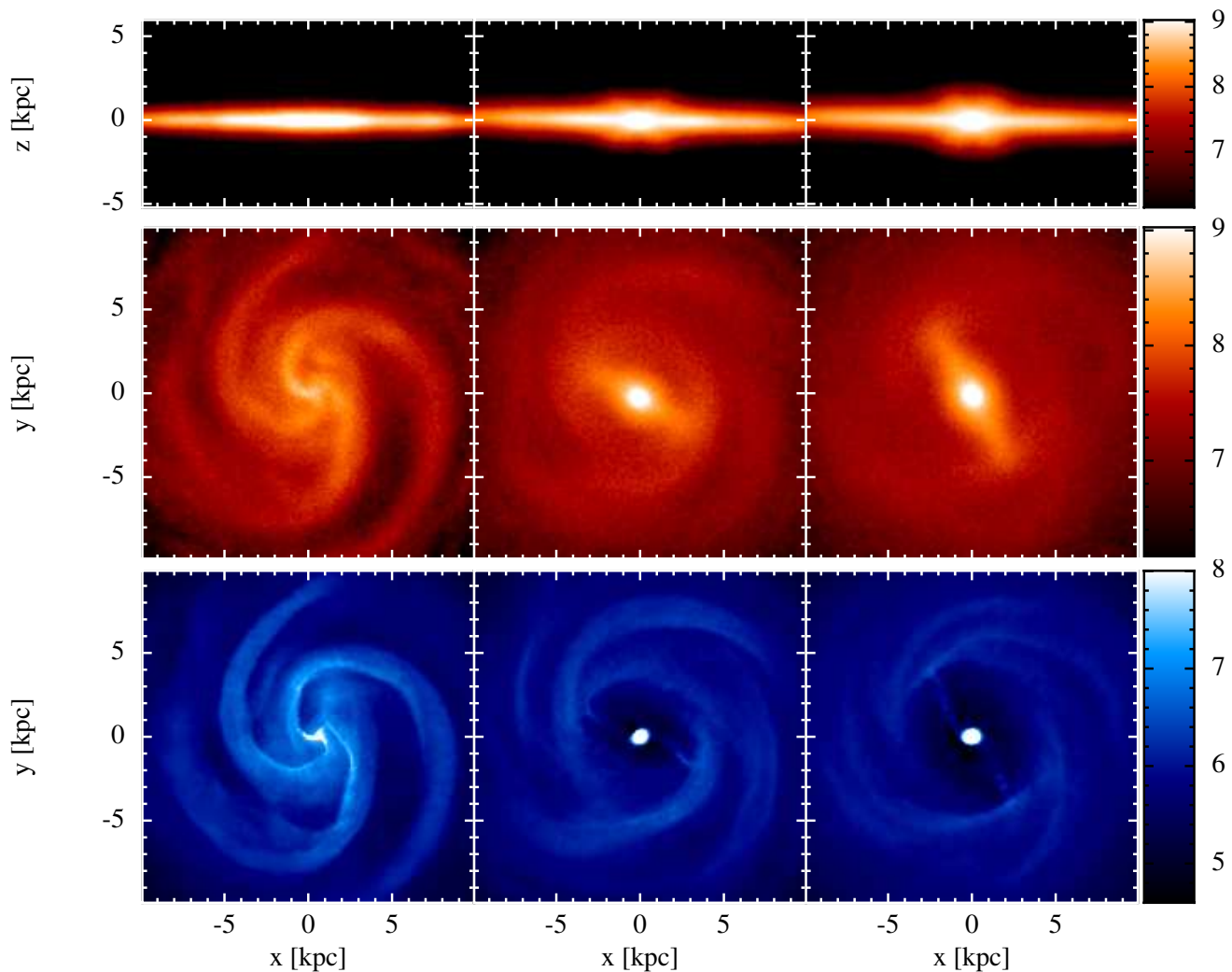


**Figure 3.** Upper (middle) panels: edge-on (face-on) views of the stellar disc at  $t = 1, 4$  and  $7$  Gyr (left, central and right panel, respectively). The colour gradient maps the stellar surface density (in units of  $M_{\odot} \text{ kpc}^{-2}$ ) on a logarithmic scale. Bottom panels, same as the middle panel for the gas surface density.

( $R_{\text{OLR}}$ ).<sup>6</sup> However, it is instead the formation of the bar which is efficient in driving substantial gas inflow. The fundamental importance of the torques acting on the gas during the build-up of the bar, before this has been fully developed, is highlighted in the right panel of figure 5, in which we show the gas accretion rate  $\dot{M}$  within  $R_C$  as a function of time. In particular, the red and blue lines refer to  $\dot{M}$  through surfaces at  $0.3$  and  $1$  kpc from the centre, respectively. At both scales  $\dot{M}$  shows a first prominent peak at  $t \approx 1$  Gyr, well before the formation of any significant bar-like structure. A second peak of similar magnitude is observable at  $t \approx 2$  Gyr, just after the bar has formed, while the central fueling drops immediately afterward. Although our simple simulation does

not include any star formation prescription, such omission has little impact on the evolution of the gas from  $R_C$  down to the nuclear knot, since the majority of the inflow happens on a few (up to  $\approx 10$  close to  $R_{\text{ILR}}$ ) orbital timescales. The time evolution of the accretion flows through the two surfaces is quite similar at all times.

### 3.2 Viscosity test

As recently reviewed by Sellwood (2014), the gas angular momentum transport in SPH simulations could be at least partially affected by the artificial viscosity used. Differently from grid based codes, in which a numerical viscosity is intrinsically related with the discretization of the space domain, in SPH codes the numerical viscosity is explicitly taken into account through a viscosity parameter  $\alpha$ . The

<sup>6</sup> Although harder to be noticed in a log-log plot, the gas surface density decreases in the  $R_C < R < R_{\text{OLR}}$  region, and the material accumulates just outside  $R_{\text{OLR}}$ .



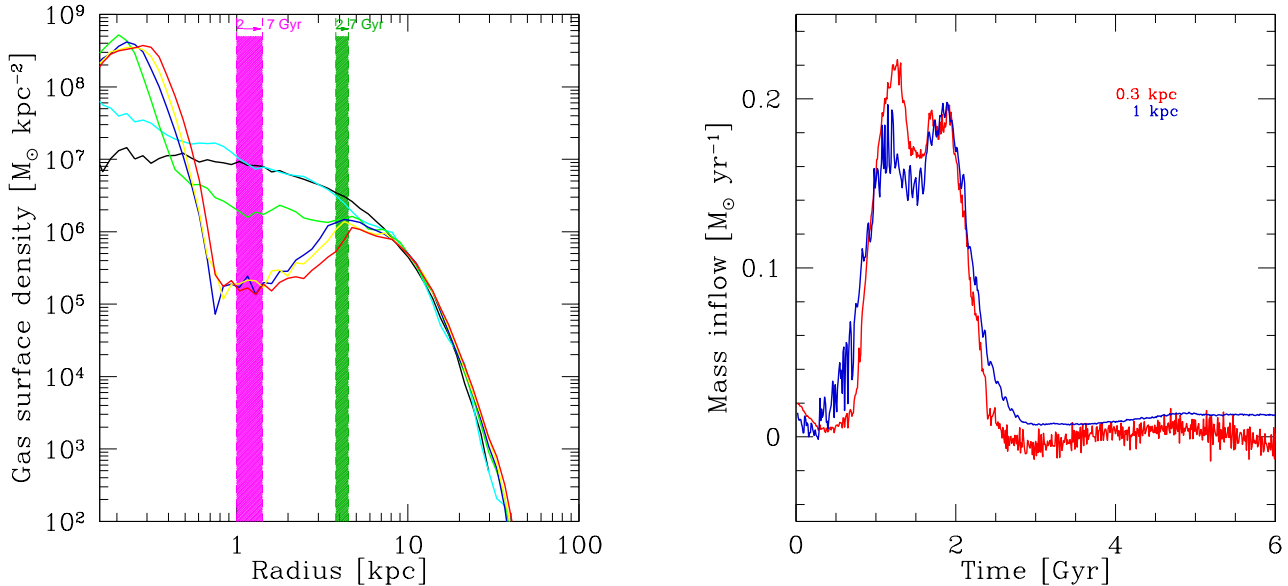


**Figure 5.** Left panel: surface density profile of the gaseous component. Solid black, cyan, green, blue, yellow and red curves correspond to  $t=0, 1, 2, 3, 5$  and  $7$  Gyr, respectively. The shaded magenta and green areas mark the region span by  $R_{\text{ILR}}$  and  $R_C$ , respectively. Right panel: gaseous mass inflow as a function of time. Red and blue lines represent the accretion rate computed at  $0.3$  and  $1$  kpc from the center respectively.

shear and bulk viscosity in SPH simulations scale linearly with  $\alpha$  (e.g. Murray 1996; Lodato & Price 2010).

In this section we test the effect of the artificial viscosity through the comparison of run LR with three different simulations. Two of these, LRV04 and LRV16, are exact copies of the LR run, but for the value of the  $\alpha$  parameter, that is half and double of the  $\alpha = 0.8$  value used in LR. The third simulation (LRGiz) has been run using the GIZMO code (Hopkins 2014), that solves the evolution of the gas on an unstructured grid and does not require any explicit artificial viscosity term.

The results of the test are shown in figure 6 and figure 7. Figure 6 shows the comparison between the surface density profiles of the four runs (LR in red, LRV16 in green, LRV04 in blue and LRGiz in cyan) at four different times,  $t=1$  Gyr (upper left panel),  $3$  Gyr (upper right panel),  $5$  Gyr (lower left panel) and  $7$  Gyr (lower right panel). Similarly, figure 7 shows the face-on projection of the gas surface density map for the four runs at  $t=1$  Gyr, to allow for a comparison of the non-axisymmetric structures forming. The comparison between the three SPH runs shows that the exact value of the viscosity parameter  $\alpha$  plays a little role in the gas dynamics. The removal of gas from the forming dead zone and the formation of a dense central gas knot are completely dominated by the gravitational torques due to the formation of non-axisymmetric structures. The LRGiz run shows some very minor differences too.

### 3.3 High resolution simulations

#### 3.3.1 Low vs high resolution run comparison

As a final test, we ran an increased resolution version of the LR simulation (HR), as discussed in section 2. Because of the higher spatial resolution and of the isothermal equation of

state implemented, the gas in the HR run forms extremely dense and compact clouds in the galaxy nucleus, slowing down the simulation enormously after the first episode of major gas inflow. For this reason we have run the HR simulation only up to  $t \approx 3$  Gyr, and we limit our analysis to the response of the gas to the initial spiral and bar formation.

Fig. 8 shows the face-on views of the stellar (left panels) and gaseous (right panels) surface density. Similarly to the low resolution simulation, during the first Gyr, the system develops stellar spiral arms (upper left panel) which evolve in a stable bar like structure (lower left panel) at about  $t=2.5$  Gyrs. The gas follows a similar dynamics as observed in the lower resolution runs, following the stellar spiral arms during the first evolutionary phase and being driven toward the centre during and after the bar formation. As in the other runs, in the central region of the galaxy (within the bar extent) a dead zone forms, with very low density gas present in between the outer disc and the nuclear gas knot.

Figure 9 shows a comparison between HR and LR runs. The left panel shows the gas surface density profiles in the two runs for four different times. The biggest difference is observable at  $t \approx 1$  Gyr, when in the low resolution run the disc is already significantly perturbed, while in the HR run the gas profile is still quite unperturbed. The gas profile in the high resolution run is more similar to its low resolution analogous at later times, but for a slightly more pronounced dead zone in the HR run due to the better resolved profile of the stellar bar, that results in a more effective action of the bar itself onto the gas.

The main difference observed in the profiles at  $t \approx 1$  Gyr is due to the later growth of non-axisymmetric perturbations (first in the form of spiral arms, turning into a central bar) in the higher resolution simulation. This is clearly observable in the accretion rate through the central  $0.3$  kpc (right panel of figure 9). In run HR the peak of  $\dot{M}$  occurs at  $t \approx 1.5$  Gyr,

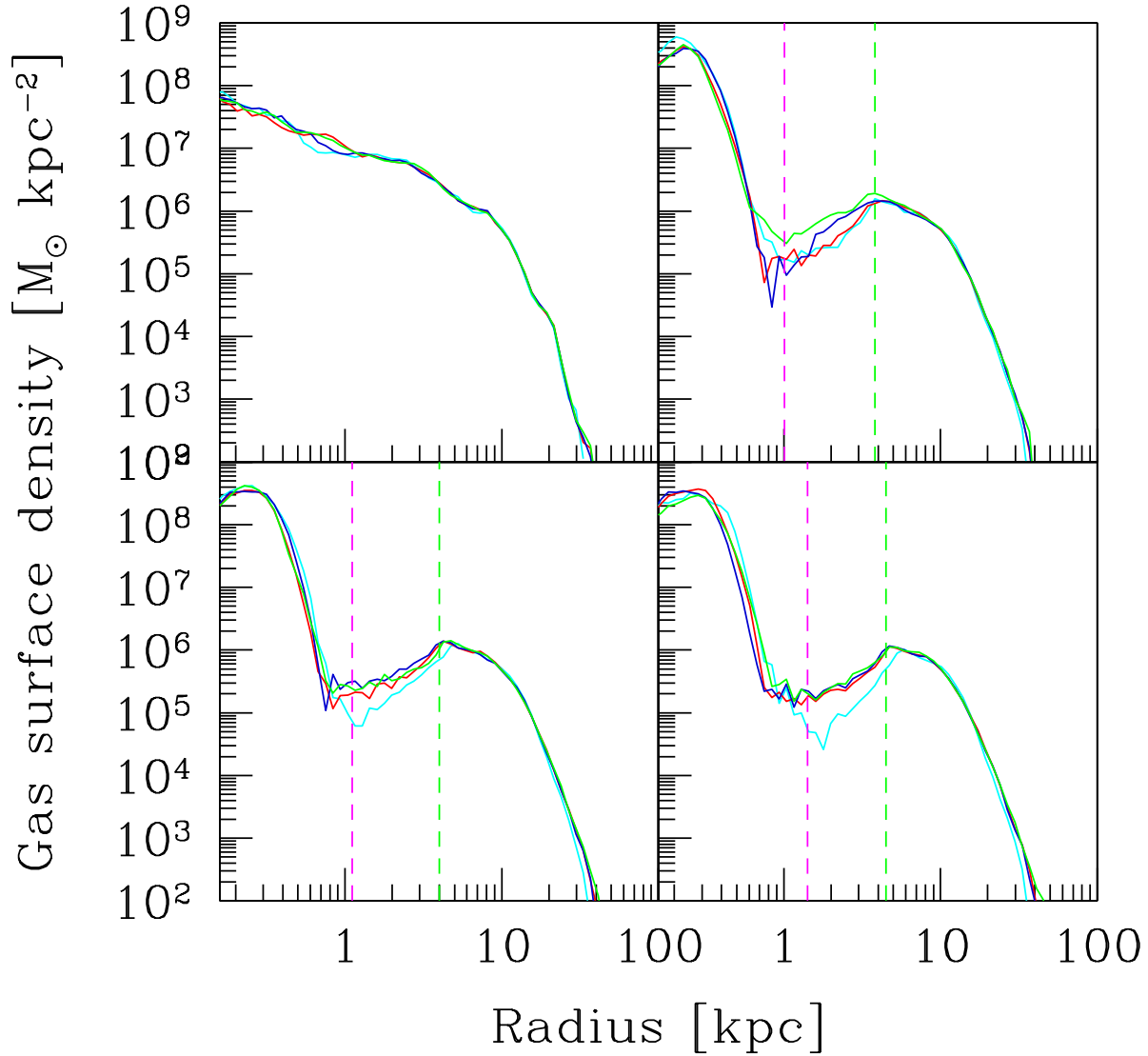


**Figure 6.** Surface density profile for low resolution isothermal simulations with different viscosity. Upper left, upper right, lower left and lower right panels refer to  $t=1$  Gyr, 3 Gyrs, 5 Gyrs and 7 Gyrs, respectively. The solid red, green and blue curves are obtained from the gas particle distribution for simulation with  $\alpha = 0.8$  (run LR),  $\alpha = 1.6$  (run LRV16) and  $\alpha = 0.4$  (run LRV04). The cyan curve corresponds to the gas particle distribution for simulation using GIZMO (LRGiz). The dashed magenta and green lines mark the positions of  $R_{\text{ILR}}$  and  $R_C$  at the different times.

about 0.2-0.3 Gyr after the peak observed in the LR run. Again, in the high resolution simulation the  $\dot{M}$  peak has a larger intensity (by almost a factor of 2) with respect to the low resolution case, due to the more efficient cleaning of the dead zone during the bar formation process.

The later growth of non-axisymmetric structures in the higher resolution run is probably due to the lower shot noise in the initial conditions: a higher number of particle MonteCarlo sampling results in a lower statistical noise, from which structures can grow (see also the discussion in Sellwood 2014). An extensive and time consuming study aiming at numerical convergence is neither feasible (within the currently available computational facilities) nor useful,

as a simulation with a order of magnitudes larger number of particles could result in a degree of symmetry significantly larger than any real disc galaxy observed. The dependence of the  $\dot{M}$  peak and of the time at which spirals and bars form on the number of particles used demonstrate that these should not be taken as physical values. Only the gas response pattern is similar in all the runs analyzed, independently of the viscosity prescription adopted, of the numerical resolution achieved, and of the algorithm used to solve the gas dynamics.



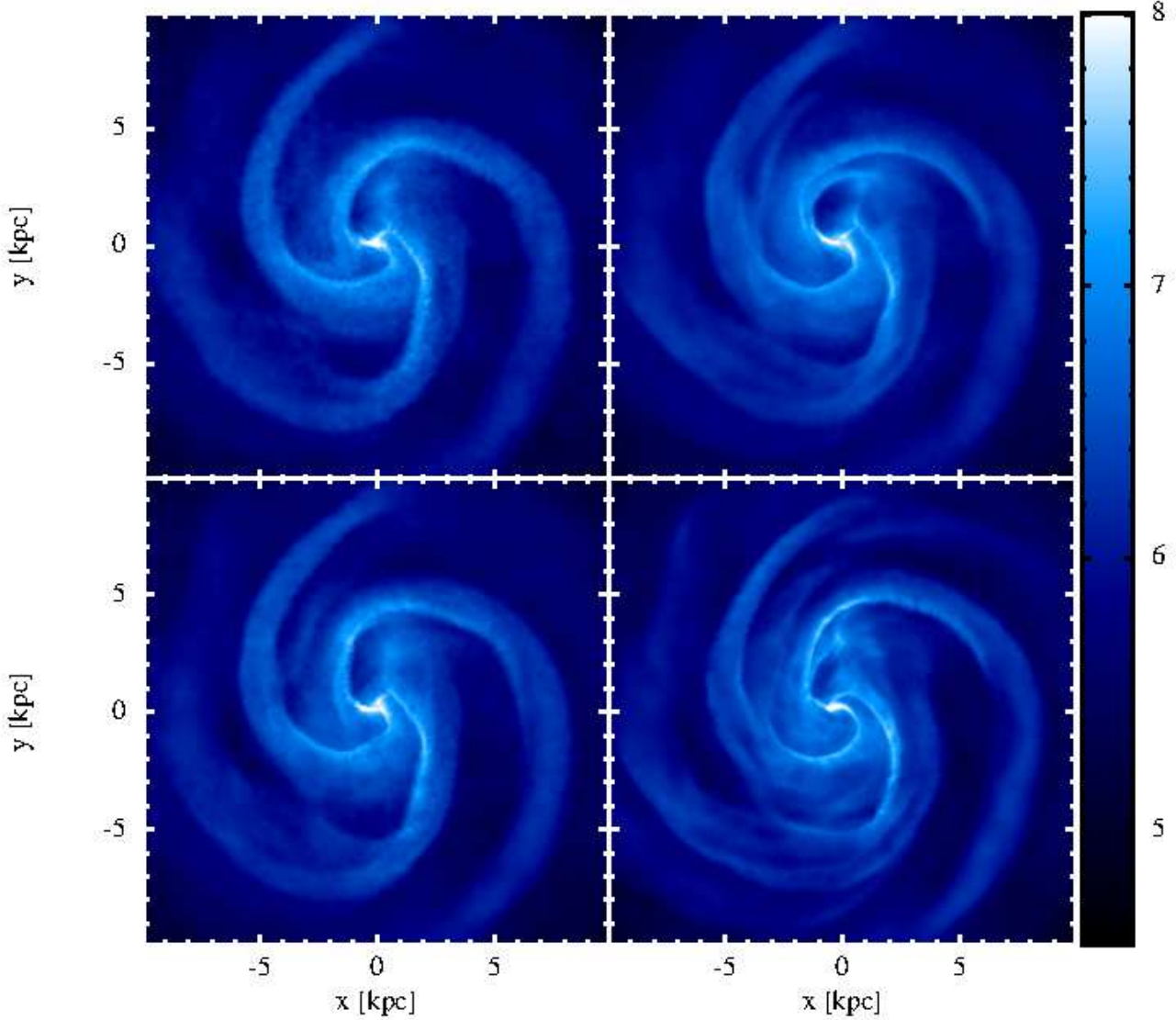


**Figure 7.** Face-on views of gas surface density for low resolution simulations with different values of  $\alpha$  at  $t=1$  Gyr:  $\alpha=0.4$  in the left upper panel,  $\alpha=1.6$  in the right upper panel,  $\alpha=0.8$  in the left lower panel and low resolution simulation using GIZMO in the right lower panel. The logarithmic density scale is in units of  $M_{\odot} \text{ kpc}^{-2}$ .

### 3.3.2 Dynamics of the nuclear inflow

The high resolution achieved allows us to resolve sub-kpc scales, and to investigate the detailed causes of the nuclear gas inflow through the search of stellar and gaseous nuclear structures. In this section we focus on two times, just before (0.8 Gyr) and right at the beginning (1.1 Gyr) of the major gas inflow event. The properties of the stellar and gaseous distribution at the two times are highlighted in the upper and lower panels of figure 10.

The left panels represent the surface density contrast for the stars within the inner 3 kpc, defined as:

$$\delta_{\Sigma_*}(R, \phi) = \frac{\Sigma_*(R, \phi) - \langle \Sigma_*(R, \phi) \rangle_{\phi}}{\langle \Sigma_*(R, \phi) \rangle_{\phi}}, \quad (9)$$

where  $R$  and  $\phi$  are the radial and azimuthal coordinates on the disc equatorial plane,  $\Sigma_*(R, \phi)$  is the stellar surface density and  $\langle \Sigma_*(R, \phi) \rangle_{\phi}$  is the average stellar surface density

evaluated in annuli. The central panels show the gas density contrast

$$\delta_{\rho, \text{gas}}(R, \phi) = \frac{\rho_{\text{gas}}(R, \phi) - \langle \rho_{\text{gas}}(R, \phi) \rangle_{\phi}}{\langle \rho_{\text{gas}}(R, \phi) \rangle_{\phi}}, \quad (10)$$

evaluated on the disc mid-plane. The right panels show the intensity of the radial motions in  $\text{km s}^{-1}$ .

Before the major inflow event (upper left panel) a single three arm spiral structure is visible down to scales of about 300 pc. The gas is affected by the stellar non-axisymmetric structure and develops shocks at the edge of the stellar spirals, as observable in density contrast map (upper central panel). Clear shock fronts develop in the gas distribution, the gas dynamics is perturbed and radial motions are triggered (upper right panel).

A different picture is present at the triggering of the strong gas inflow episode (lower panels). At  $t = 1.1$  Gyr the inner part (within  $\approx 1$  kpc) of the stellar three arm spiral

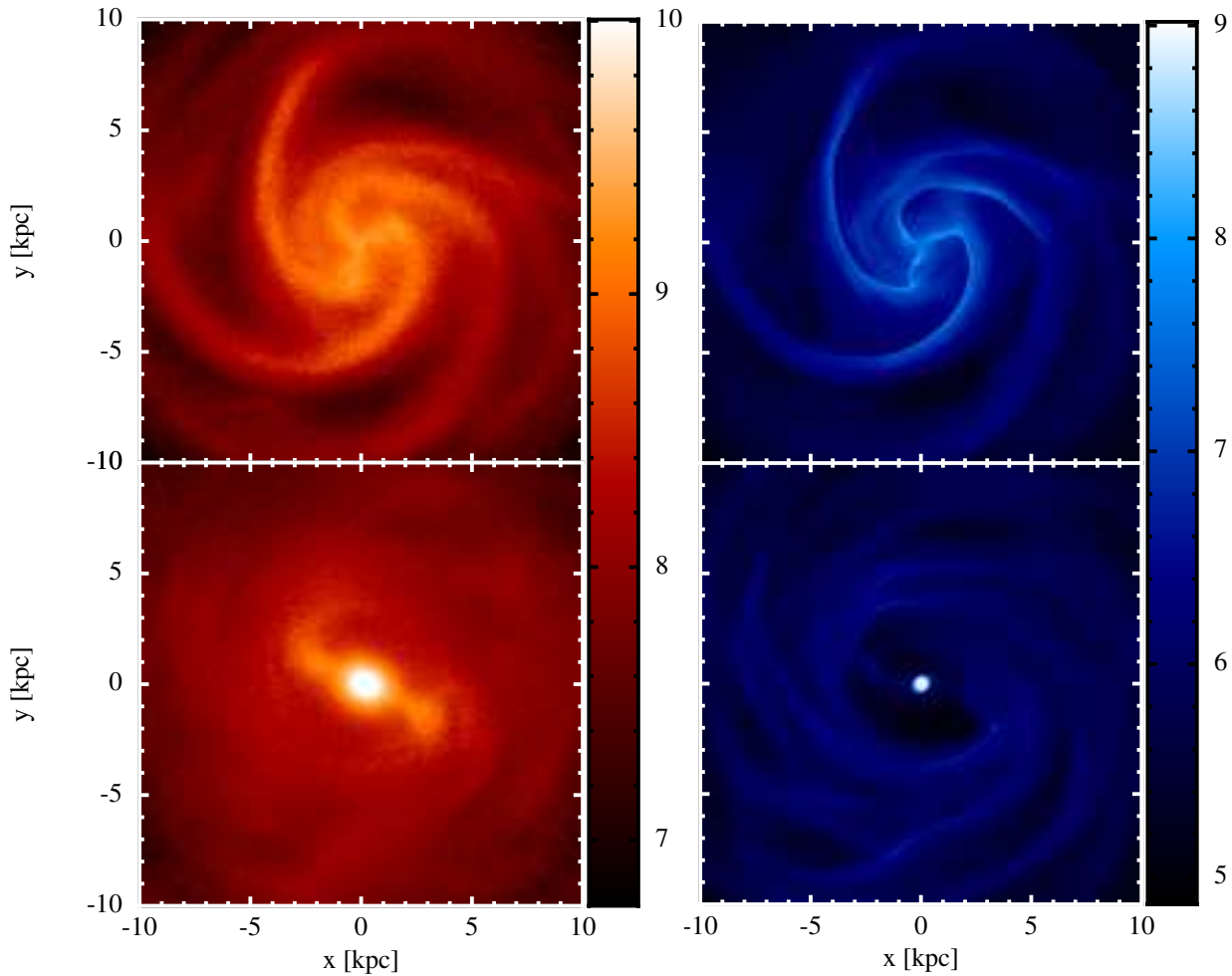


**Figure 8.** Right panels: logarithmic face-on views of the stellar surface density (in unit of  $M_{\odot} \text{ kpc}^{-2}$ ) for the high resolution simulation (HR) at  $t = 1$  Gyr (upper panel) and  $t = 2.5$  Gyr (lower panel). Left panels: same as right panels for the gas surface density.

structure decouples from the outer spiral structure, still evident at large scales ( $\sim 3$  kpc), as clearly visible in the lower left panel. Such decoupled structure is clearly observable in the gas density (lower central panel) map. The interplay between the outer and inner spiral structure increases the radial velocity of the gas in the central regions as well as the region participating to the radial inflow (lower right panel). The effect of the inner spiral decoupling onto the gas is reminiscent of the bars-within-bars scenario, originally proposed by Shlosman, Frank & Begelman (1989), in its “*stuff-within-stuff*” version (Hopkins & Quataert 2010), where the gravitational torques acting onto the gas are caused by non-axisymmetric structures not necessarily bar-like.

By the time a clear bar forms, all the gas affected by the nuclear spirals formed the central nuclear knot.

As a final comment, we stress that the nuclear regions of our galaxy do not show any evidence of gaseous clumps, whose migration could, in principle, cause the major gas inflow event (e.g. Bournaud, Elmegreen & Elmegreen 2007; Elmegreen, Bournaud & Elmegreen 2008). As a matter of fact, the further inwards one goes, the less evidence one has for clump formation. Such trend is not unexpected in systems with small gas-to-stellar mass fraction as the one we

study here, that remains locally stable throughout the whole duration of the runs.

### 3.3.3 Nuclear disc

We devote the last part of our analysis to the structure of the gas nuclear structure forming during the major inflow event. In particular we will focus on the gas properties well after the nuclear structure formed and reached a stable configuration.

Figure 11 shows the density contrast of gas in the inner 3 kpc (left panel) and in the inner 400 pc (middle panel), and the radial velocity map (right panel) at about 2.5 Gyr. The orientation of the bar is traced by the inflowing streams of gas that connect the outer regions of the galaxy with the inner gaseous structure. The gas in the inner few hundreds of pc forms a rotating disc. Within the disc nuclear spirals are observable down to few tens of pc, traced by local gaseous overdensities (lighter regions in the central panel) corresponding to inflowing gas (blue and green regions in the right panel). A careful analysis of the stellar distribution does not show any central structure (neither in the form of spirals nor of bar). We therefore interpret the central two armed spirals as the effect that the outer bar has onto the

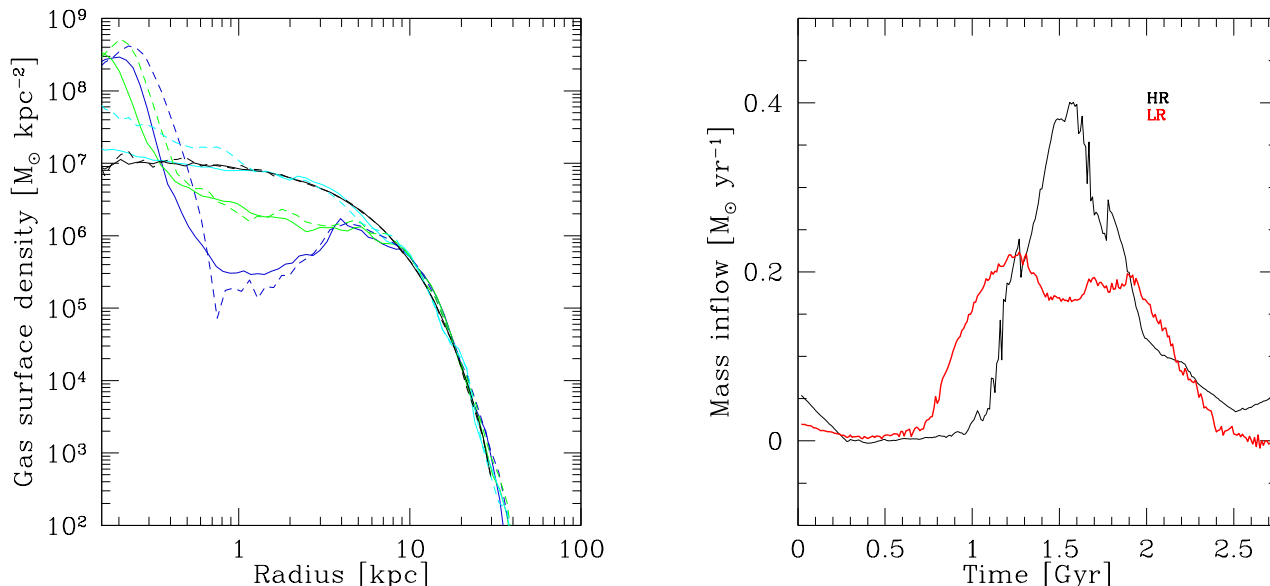


**Figure 9.** Left panel: surface density profile of the gas. Solid lines refer to the highest resolution run HR. The results of the low resolution run LR are reported with dashed lines for comparison. Black, cyan, green and blue curves refer to  $t = 0, 1, 2$ , and  $3$  Gyr, respectively. Right panel: gaseous mass inflow as a function of time. Black and red lines represent the inflow rate computed at  $0.3$  kpc from the center in run HR and LR respectively.

gas within its ILR, as discussed analytically in Maciejewski (2004a) and observed in numerical simulations of the response of gas to a bar-like analytical potential (Maciejewski 2004b).

As a note of caution we stress that the accretion rate at late times and, more in general, the long-term evolution of the central gaseous concentration would be significantly different if the gas would be allowed to form stars, possibly forming a pseudo-bulge like structure. We plan to study the possible effect of star formation on the nuclear scale gas dynamics in a future investigation.

#### 4 DISCUSSION AND CONCLUSIONS

In this paper we studied the gas response to the formation and evolution of a stellar bar in an isolated disc galaxy. The galaxy is initially unstable to the formation of non-axisymmetric structures and develops multiple spiral arms in the first Gyr, that evolve in a central stellar bar at  $t \sim 2$  Gyr. The forming bar slows down with time, and buckles in its central  $\gtrsim$  kpc region.

During the first spiral arm dominated phase the gas, forced by the stellar potential, forms clearly defined spiral arms. During this phase a major episode of gas inflow takes place, larger by a factor of  $\gtrsim 3$  than any other inflow event after the bar formation. The analysis of the higher resolution simulation shows that the trigger of the major inflow is the decoupling of the nuclear regions of the three armed spiral from the outer counterpart. At later times, when the stellar bar is already established, a low gas density annulus (here defined as the dead zone) between the bar corotational and the inner Lindblad resonances  $R_{\text{ILR}} \lesssim R \lesssim R_C$  is clearly observable in the simulations. We notice that such a gas depleted region is often observed in local samples of barred

spiral galaxies, as extensively discussed in Gavazzi et al. (2015).

We checked our results against the numerical viscosity used, and we demonstrated that the gas dynamics is little affected by the exact value of the viscosity parameter in the SPH runs, and by the exact hydrodynamical treatment of the gas. We also studied the dependence of our results on the numerical resolution. We found that, although the qualitative evolution of the gas is resolution independent, the exact time at which the non axisymmetric structures develop and the actual maximum inflow rate at small (but completely resolved) scales do depend on the resolution achieved. As discussed above, the difference in the timescales for the inflow and for the bar formation are probably due to a lower shot noise in the highest resolution initial conditions. The difference in the magnitude of the maximum inflow rate, instead, is due to the fact that the bar itself as well as all the non-axisymmetric structure are better resolved in the highest resolution run, resulting in a more effective torquing of the gas.

Independently of the exact numerical implementation, we find that the flux of gas reaching the most central regions of the galaxy peaks during the bar formation phase, and not when the bar is fully established. The explanation of such result is twofold: (1) since bars are quite efficient in driving the gas within their corotational radius toward the centre, after few bar orbits the central region of the galaxy is mostly gas free (as already noted by Berentzen et al. 1998), and there is no remaining gas to be torqued by the bar; (2) in our simulations the forming bar slows down as the galaxy evolves, increasing its ILR and corotational radii (in agreement with, e.g. Sellwood 1981; Combes & Sanders 1981; Halle et al. 2015). As a consequence, the gas that is perturbed by the early fast-precessing bar reaches regions significantly more nuclear than gas perturbed at later times.



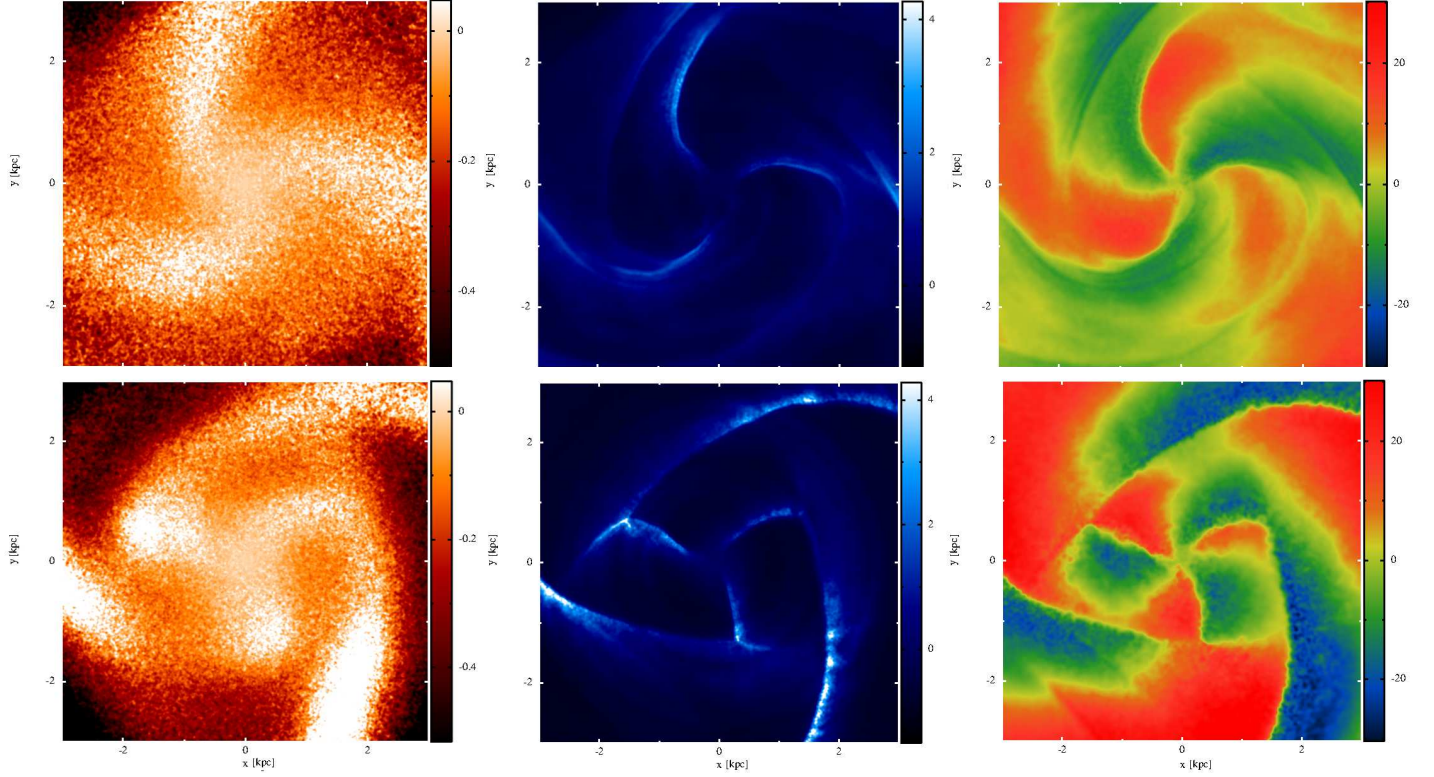


**Figure 10.** Upper panels: stellar surface density contrast (left), gas density contrast (middle) and radial velocity map (right, in unit of  $\text{km s}^{-1}$ ) for gas in the inner 3 kpc at  $t=0.8$  Gyr. Lower panels: same as the upper panels at  $t = 1.1$  Gyr. See text for details.

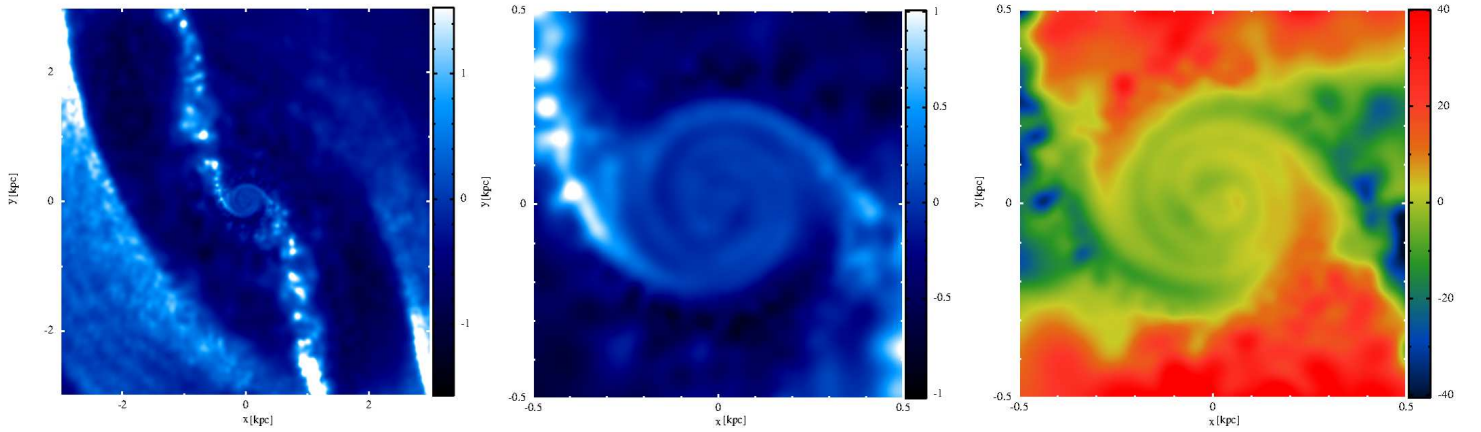


**Figure 11.** Gas density contrast in the inner 3 kpc (left panel) and 500 pc (central panel). The right panel shows the radial velocity for gas (in unit of  $\text{km s}^{-1}$ ) in the inner 500 pc at 2.5 Gyrs. See text for details.

The low efficiency of large, long-lived and easy to spot bars in fueling the very central regions of galaxies can explain why many observational studies do not find significant links between bars and AGN activity. The high efficiency of the *bar formation* process in driving strong inflows toward the very central region of galaxies hints, on the other hand, at a possibly underestimated importance of bar driven AGN activity in disc galaxies.

Finally, the analysis of the long lived nuclear gaseous disc shows that the outer, large scale, bar keeps on exerting a dynamical effect onto the gas within few hundreds of pc.

A two armed spiral can be observed both in the gas density distribution and in the gas dynamics, as already discussed by Maciejewski (2004a) and Maciejewski (2004b).

As a final note of caution, we highlight the main shortcoming of the simulation suite discussed here:

(i) Our simulations lack physically motivated prescriptions for gas radiative cooling, star-formation and any star-formation-related feedback, as well as accretion onto a possibly present massive black hole and the related AGN feedback. We stressed that the dynamics of the gas in the region studied here (down to few hundred pc from the galaxy cen-

tre) is not strongly affected by the lack of additional physics, as the gas inflow happens on few orbital timescales. As a matter of fact, we regard the lack of additional physics as a plus in our runs, as it allows to clearly highlight the dynamical processes ongoing in the simulation in a controlled system. On the other hand, the lack of star formation and related feedbacks does not allow us to draw firm conclusions about the long term evolution of the gas at small scales, as a significant fraction of the gas could turn into stars on the Gyr timescales of the simulations. A follow up set of runs including additional physics is currently in preparation;

(ii) All the simulations discussed here share the same idealized initial conditions. We regard this as the main drawback of our study. Because of this we cannot use our runs to make any general prediction about barred galaxies in general. We stress, however, that our simple runs do highlight the possible relevance of early gas inflow during the bar formation phase. We plan to check our results with fully evolving isolated galaxy simulations starting from different initial conditions and, with a considerable increase of the computational cost, with cosmological simulations.

## ACKNOWLEDGMENTS

We thank the anonymous Referee for her/his suggestions that significantly improved the quality of the paper. We acknowledge Alessandro Lupi for the help in the technical aspects of the runs, and for his comments on the paper. We further thank Silvia Bonoli, Pedro R. Capelo, Guido Consolandi, Jorge Cuadra, Roberto Decarli, and Giuseppe Gavazzi for their comments and insights.

## References

- Alonso M. S., Coldwell G., Lambas D. G., 2013, *A&A*, 549, A141
- Athanassoula E., 1992, *MNRAS*, 259, 345
- Balsara D. S., 1995, *Journal of Computational Physics*, 121, 357
- Barnes J., Hut P., 1986, *Nature*, 324, 446
- Berentzen I., Heller C. H., Shlosman I., Fricke K. J., 1998, *MNRAS*, 300, 49
- Berentzen I., Shlosman I., Martinez-Valpuesta I., Heller C. H., 2007, *ApJ*, 666, 189
- Binney J., Tremaine S., 2008, *Galactic Dynamics: Second Edition*. Princeton University Press
- Bournaud F., Elmegreen B. G., Elmegreen D. M., 2007, *ApJ*, 670, 237
- Cheung E. et al., 2015, *MNRAS*, 447, 506
- Cisternas M. et al., 2013, *ApJ*, 776, 50
- Cole D. R., Debattista V. P., Erwin P., Earp S. W. F., Roškar R., 2014, *MNRAS*, 445, 3352
- Combes F., Sanders R. H., 1981, *A&A*, 96, 164
- Elmegreen B. G., Bournaud F., Elmegreen D. M., 2008, *ApJ*, 688, 67
- Fiacconi D., Feldmann R., Mayer L., 2015, *MNRAS*, 446, 1957
- Gavazzi G. et al., 2015, arXiv:1505.07836
- Goz D., Monaco P., Murante G., Curir A., 2014, arXiv:1412.2883
- Halle A., Di Matteo P., Haywood M., Combes F., 2015, arXiv:1501.00664
- Hernquist L., 1990, *ApJ*, 356, 359
- Hernquist L., 1993, *ApJS*, 86, 389
- Hinshaw G. et al., 2013, *ApJS*, 208, 19
- Ho L. C., Filippenko A. V., Sargent W. L. W., 1997, *ApJ*, 487, 591
- Hopkins P. F., 2014, arXiv:1409.7395
- Hopkins P. F., Quataert E., 2010, *MNRAS*, 407, 1529
- Hunt L. K., Malkan M. A., 1999, *ApJ*, 516, 660
- Jogee S., Scoville N., Kenney J. D. P., 2005, *ApJ*, 630, 837
- Kim W.-T., Seo W.-Y., Kim Y., 2012, *ApJ*, 758, 14
- Knapen J. H., Shlosman I., Peletier R. F., 2000, *ApJ*, 529, 93
- Komatsu E. et al., 2011, *ApJS*, 192, 18
- Kormendy J., 2013, *Secular Evolution in Disk Galaxies*, Falcón-Barroso J., Knapen J. H., eds., p. 1
- Kraljic K., Bournaud F., Martig M., 2012, *ApJ*, 757, 60
- Laine S., Shlosman I., Knapen J. H., Peletier R. F., 2002, *ApJ*, 567, 97
- Laurikainen E., Salo H., Buta R., 2004, *ApJ*, 607, 103
- Lee G.-H., Park C., Lee M. G., Choi Y.-Y., 2012a, *ApJ*, 745, 125
- Lee G.-H., Woo J.-H., Lee M. G., Hwang H. S., Lee J. C., Sohn J., Lee J. H., 2012b, *ApJ*, 750, 141
- Lodato G., Price D. J., 2010, *MNRAS*, 405, 1212
- Maciejewski W., 2004a, *MNRAS*, 354, 883
- Maciejewski W., 2004b, *MNRAS*, 354, 892
- Martinet L., Friedli D., 1997, *A&A*, 323, 363
- Mayer L., Wadsley J., 2004, *MNRAS*, 347, 277
- Mo H. J., Mao S., White S. D. M., 1998, *MNRAS*, 295, 319
- Monaghan J. J., 1992, *ARA&A*, 30, 543
- Monaghan J. J., 1997, *Journal of Computational Physics*, 136, 298
- Mulchaey J. S., Regan M. W., 1997, *ApJ*, 482, L135
- Murray J. R., 1996, *MNRAS*, 279, 402
- Nair P. B., Abraham R. G., 2010, *ApJ*, 714, L260
- Navarro J. F., Frenk C. S., White S. D. M., 1996, *ApJ*, 462, 563
- Navarro J. F., Frenk C. S., White S. D. M., 1997, *ApJ*, 490, 493
- Oh S., Oh K., Yi S. K., 2012, *ApJS*, 198, 4
- Regan M. W., Sheth K., Vogel S. N., 1999, *ApJ*, 526, 97
- Regan M. W., Teuben P. J., 2004, *ApJ*, 600, 595
- Roberts, Jr. W. W., Huntley J. M., van Albada G. D., 1979, *ApJ*, 233, 67
- Romano-Díaz E., Shlosman I., Heller C., Hoffman Y., 2008, *ApJ*, 687, L13
- Sanders R. H., Huntley J. M., 1976, *ApJ*, 209, 53
- Scannapieco C., Athanassoula E., 2012, *MNRAS*, 425, L10
- Sellwood J. A., 1981, *A&A*, 99, 362
- Sellwood J. A., 2014, *Reviews of Modern Physics*, 86, 1
- Shlosman I., Frank J., Begelman M. C., 1989, *Nature*, 338, 45
- Springel V., 2005, *MNRAS*, 364, 1105
- Springel V., Di Matteo T., Hernquist L., 2005, *MNRAS*, 361, 776
- Springel V., Hernquist L., 2002, *MNRAS*, 333, 649
- Villa-Vargas J., Shlosman I., Heller C., 2010, *ApJ*, 719, 1470
- Wada K., 2001, *ApJ*, 559, L41
- Wada K., Norman C. A., 2001, *ApJ*, 547, 172